Department of Physics and Astronomy

Heidelberg University

Bachelor Thesis in Physics

submitted by

Lisa Eileen Moraw

born in Aschaffenburg, Germany

2024

Vacuum System Optimization

for an Enhanced Metastable Argon Flux

for ATTA

This Bachelor thesis has been carried out by Lisa Eileen Moraw

at the

Kirchhoff-Institute for Physics

under the supervision of

Prof. Dr. Markus Oberthaler

Abstract

A deeper understanding of hydrological systems requires the resolution of time scales, which can be achieved by investigating radioisotope tracers. Argon Trap Trace Analysis provides a technology to detect the extremely rare isotope ^{39}Ar by single atom counting. Due to its half-life of 268(8) years, this isotope bridges a gap in dating capabilities inaccessible to other tracers and finally enables a routine application for environmental studies. The measurement precision directly correlates with the count rate of metastable ^{39}Ar, which is partly limited by collisions with background gas, causing deexitation of scattered atoms. Accordingly, measurements show a reduction in the metastable flux for higher pressures. In order to investigate optimization of the vacuum system towards less scattering of atoms, atom flux measurements were executed at two positions along the beam axis. Vacuum system configurations are varied in between an absorption spectroscopy and an absolute flux measurement in the source and quench chamber, respectively. The data indicates a possible improvement by exchanging the former differential pumping tube with a less flow restricting setup and thus avoiding pressure peaks along the beam axis. However, even though significant differences were observed for the different setups, the processes behind are not fully understood and a more complete model is yet to be determined. Having carried out this thesis with only the front part of the vacuum system, future work is needed to determine the effects on the whole ArTTA-apparatus.

Zusammenfassung

Ein tieferes Verständnis für hydrologische Systeme erfordert die Auflösung von Zeitskalen, was durch die Untersuchung radioisotopischer Spurenstoffe erreicht werden kann. Argon Trap Trace Analysis bietet eine Technologie zum Nachweis des sehr seltenen Isotops ^{39}Ar durch Einzelatomzählung. Aufgrund seiner Halbwertszeit von 268(8) Jahren schließt dieses Isotop eine für andere Spurenstoffe nicht auflösbare Lücke in den Datierungsmöglichkeiten und ermöglicht somit eine Routineanwendung für Umweltstudien. Die Messgenauigkeit korreliert direkt mit der Zählrate von metastabilem ^{39}Ar, die unter anderem durch Kollisionen mit dem Hintergrundgas begrenzt wird, welche zur Deexitation der gestreuten Atome führen. Dementsprechend zeigen die Messungen eine Verringerung des metastabilen Flusses für höhere Drücke. Um eine Optimierung des Vakuumsystems im Hinblick auf weniger Streuung der Atome zu untersuchen, wurden Atomflussmessungen an zwei Positionen entlang der Strahlachse durchgeführt. Die Konfiguration des Vakuumsystems wurde zwischen einer Absorptionsspektroskopie und einer Messvorrichtung des absoluten Flusses in der Quell- bzw. Quench-Kammer variiert. Die Daten deuten auf eine mögliche Verbesserung durch den Austausch der bisherigen differentiellen Pumpstufe gegen einen weniger flusslimitierenden Aufbau hin, wodurch Druckspitzen entlang der Strahlachse vermieden werden können. Obwohl signifikante Unterschiede zwischen verschiedenen Konfigurationen beobachtet wurden, sind die zugrunde liegenden Prozesse noch nicht vollständig verstanden und geben den Ausblick auf weitere Verbesserungen des Modells. Da in dieser Arbeit nur der vordere Teil des Vakuumsystems untersucht wurde, sind künftige Arbeiten erforderlich, um die Auswirkungen auf das gesamte ArTTA-System zu ermitteln.

Contents

List of abbreviations

APD avalanche photo diode

ArTTA Argon Trap Trace Analysis

ATTA Atom Trap Trace Analysis

CCD charge-coupled device

DPT differential pumping tube

LN_2 liquid nitrogen

MOL magneto-optical lens

MOT magneto-optical trap

RF radio frequency

TMP turbo-molecular pump

ZSL Zeeman slower

1 Introduction

Our environment holds many phenomena that still remain undescribed and unexplored while science seeks to gain a more and more profound knowledge by developing and testing new methods. In hydrology, tracers play a major role as they enable the description of time scales of certain processes. A tracer is a substance introduced into a system in a natural or anthropogenic way, which can be tracked as it moves or transforms within that system and hence enables to draw conclusions about the system itself.

The dating range of the noble gas radioisotope tracer argon-39 (^{39}Ar) lays between 50 and 1300 years, resulting from its half-life of 268(8) years [1, 2], and thus, covers a time scale that common tracers like ^{14}C or ^{85}Kr cannot resolve. ^{39}Ar can be used for studying groundwater systems, ocean circulation, and many more, as these systems have typical timescales that correspond to the dating range for argon. However, ^{39}Ar requires an ultra-sensitive detection method since it has a very low natural abundance of $^{39}\mathrm{Ar/Ar} = 8.1(3) \cdot 10^{-16}$ [3]. Atom Trap Trace Analysis (ATTA) is a suited method for abundances this low because it allows counting single atoms. Its application for ^{39}Ar is denoted as Argon Trap Trace Analysis (ArTTA), which is also referred to as the name of the experimental setup. The isotopic shift of quantum mechanical energy levels enables to distinguish the different isotopes, allowing the selective addressing of ^{39}Ar through implemented laser cooling. However, the atoms must first be excited to a metastable state using a plasma source in order to address it with commercially available lasers. This metastable state is sensitive to collisions with background gas, which deexcites the atoms and makes them 'lost' for counting.

This thesis focuses on the optimization of the vacuum system of ArTTA in order to maximize the metastable atom flux and hence the count rate of ^{39}Ar. The overall flux is restricted by the smallest tube diameter in the apparatus. By enlarging the diameter, the effect of enhancing the total flux competes with increasing losses due to scattering for an elevated overall pressure. For obtaining a better knowledge about the effect of scattering, within the scope of this thesis, the impact of different vacuum configurations, with changing diameters, on the atom flux was further investigated. A newly implemented absorption measurement setup monitored the initial atom flux, whereas an already existent quench flux measuring tool monitored the flux after through-passing the modified vacuum configuration.

The principle of laser cooling and further underlying fundamental physics are presented in chapter 2 which moreover provides an overview of the ArTTA-apparatus and an introduction in vacuum technology. A detailed description of the implementation of the absorption setup and the measurement procedure is denoted in chapter 3, followed by the evaluation of the measurement data in chapter 4. The analysis includes the development of a model resolving the losses in metastable atoms at a fixed position along the beam axis in the apparatus, only depending on the pressure in the source chamber. The conclusive findings of the investigation of this work as well as an outlook for further improvements of the vacuum system can be found in chapter 5.

2 Fundamentals

Understanding the interaction of atoms with light is vital for working on the ArTTA-apparatus, since the machine manipulates atoms based on their optical properties. The following section introduces the fundamental principles of laser cooling as well as the relevant energy spectrum of argon, essential for its application within the frame of Argon Trap Trace Analysis. Subsequently, an overview of the apparatus and its primary components is provided. Since this thesis focuses on optimizing the vacuum system, a brief introduction into vacuum technology is also added.

2.1 Interaction of atoms with light

The interaction of atoms and photons bases on absorption and emission processes. As laser cooling constitutes one of the primary mechanisms employed in ArTTA, the underlying principles of the Doppler shift, Zeeman shift and optical molasses are introduced in the following.

2.1.1 Transitions

The energy of a photon is defined by the Planck constant h and its frequency f:

$$E = hf. \tag{2.1}$$

The momentum $\vec{p}$ of a photon is determined by the product of $\hbar = h/(2\pi)$ and the wave vector $\vec{k}$ of the photon:

$$\vec{p} = \hbar\vec{k}. \tag{2.2}$$

Examining a simple two-level quantum system, the principles of absorption, spontaneous emission and stimulated emission will be explained in the following. A two-state atom has two energy levels: a ground state with lower energy and an excited state with higher energy. An interaction between a photon and an atom takes place when the energy of the incoming photon is in the same range as the difference between the two energy levels. The probability of the interaction decreases with increasing deviation [4]. The three processes are illustrated in figure 1.

Absorption can occur if the atom is in the ground state. As an incoming photon is absorbed by the atom, the electron is lifted from the ground state to the exited state by taking the energy of the incoming photon. Due to the law of momentum conservation, the momentum of the atom changes by $\hbar\vec{k}$. This implies that stimulated absorption induces a repulsion of the atom in the direction of the photon's propagation, exerting a force proportional to the momentum of the photon.

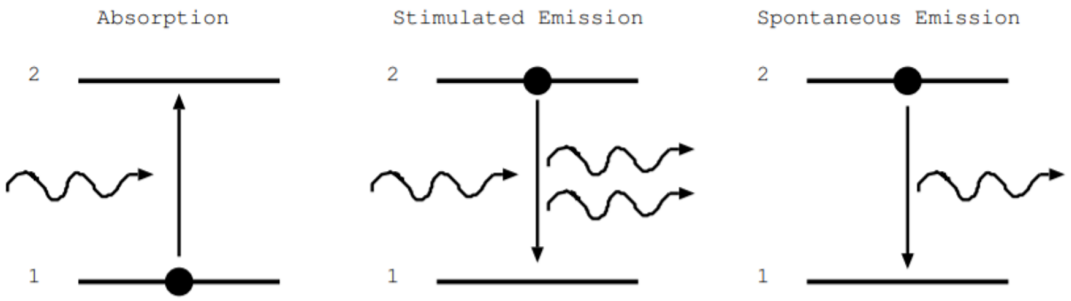

Figure 1: Demonstration of three atom-photon interactions in a two-level quantum system: absorption, spontaneous emission and stimulated emission. The numbers 1 and 2 denote the ground state and the exited state. Figure adapted from [5].

If the atom is in the excited state, an incoming photon can cause the atom to deexcite. This so called **stimulated emission** occurs when the photon's energy equals the energy gap between the two states. The electron falls back to the ground state and a photon is emitted which is coherent to the incoming photon, meaning it has the same frequency, direction, phase and electromagnetic polarisation. [5] During this process, the momentum of the atom changes by $\hbar\vec{k}$, due to the emittance of a second photon.

Spontaneous emission occurs when an atom transits from the exited state to the ground state spontaneously, meaning without external influence. It is also describes as decay process. The released energy is emitted in the form of a photon in a random direction with the momentum $\hbar\vec{k}$.
Both emission processes lead to the exertion of a repulsive force equivalent to that observed in the absorption process.

As working with lasers in the experiment, the single photon model is replaced by a laser beam. Now, many photons interact with many atoms in a short timeframe. The photon-scattering rate per atom is described by

$$\gamma_s = \frac{\gamma}{2}\frac{s_0}{1 + s_0 + (2\delta/\gamma)^2}\,, \tag{2.3}$$

where γ and s_0 denote the decay rate of spontaneous emission and the saturation parameter. $\delta = \omega_L - \omega_0$ describes the detuning between the atomic resonance frequency ω_0 and the actual laser frequency ω_L. Further information can be found in [6]. As in case of spontaneous emission, the emitted photons do not have a favoured direction, and thus, the averaged recoil over many scattering cycles is zero. On the contrary, the repulses due to stimulated absorption always act in the same direction, which is why in total, the atoms experience a net force. The force that light induced on an atom

$$\vec{F} = \gamma_s \hbar\vec{k} \tag{2.4}$$

is characterised by the momentum transfer $\hbar\vec{k}$ of a photon and the scattering rate γ_s.

2.1.2 Doppler shift

In terms of the interaction between atoms and light, so far the velocity of the atom $\vec{v}$ was not further incorporated. A smaller relative velocity, resulting from a movement of the atom in the direction of the light, leads to a reduction in wavelength and hence an increase in frequency. Similarly, if the atom is moving away from the light source, it undergoes a redshift, thus, a reduction in frequency. This frequency shift due to a change in the relative velocity between an atom and light

$$\delta_D = -\vec{k} \cdot \vec{v} \tag{2.5}$$

is denoted by the Doppler effect.

2.1.3 Zeeman shift

The Zeeman effect is an additional phenomenon that occurs in conjunction with frequency detuning. It describes the splitting of energy levels in an external magnetic field (see figure 2), whereby the respective energy shift increases linearly with the magnitude of the magnetic field B. The direction of the energy shift

$$\Delta E = \mu_B \, g_L \, m|\vec{B}| \tag{2.6}$$

depends on the algebraic sign of the magnetic quantum number m. μ_B and g_L denote the Bohr magneton and the Landé g-factor.

Consequently, by applying an external magnetic field, the transition energy between two states $|1\rangle$ and $|2\rangle$ changes and hence the corresponding resonance frequency. The detuning is labelled as Zeeman shift [6]

$$\delta_Z = (g_2 m_2 - g_1 m_1) \, \frac{\mu_B |\vec{B}|}{\hbar}. \tag{2.7}$$

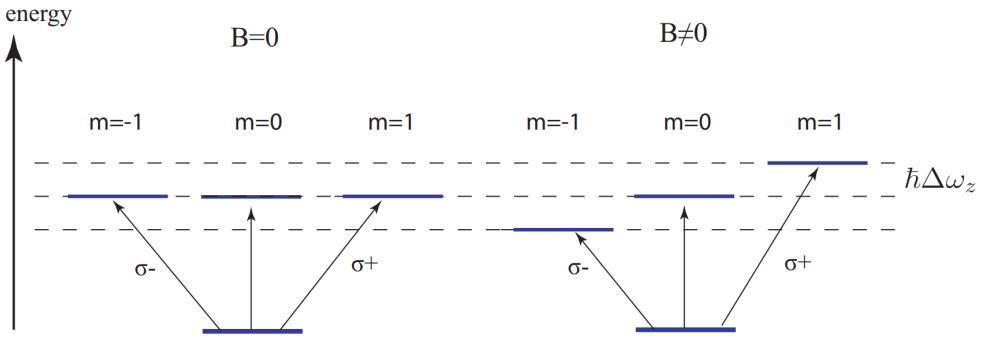

Figure 2: Demonstration of Zeeman-Splitting in a two-level quantum system with ground state and split exited state. The energy shift is indicated with $\hbar\,\Delta\omega_z$. σ^+ and σ^- describe the polarisation of the light. Figure taken from [7].

2.1.4 Optical molasses

Optical molasses are using the in eq. 2.4 introduced force for manipulating the trajectory of atoms by laser cooling. In the one-dimensional case, an atom is hit by two counter-propagating laser beams with opposite wave vectors $\vec{k}$ and $-\vec{k}$ and a detuning of δ_L. For low laser powers, which are assumed here, the atom interacts with the light only via absorption and spontaneous emission, meaning that stimulated emission can be neglected. The resulting force on a moving atom with velocity $\vec{v}$ is [6]

$$\vec{F} = \vec{F}_+ + \vec{F}_- = \frac{\gamma s_0 \hbar \vec{k}}{2} \left[\frac{1}{1 + s_0 + 4\frac{(\delta_L - \vec{k}\cdot\vec{v})^2}{\gamma^2}} - \frac{1}{1 + s_0 + 4\frac{(\delta_L + \vec{k}\cdot\vec{v})^2}{\gamma^2}} \right] \tag{2.8}$$

and is depicted in figure 3. That means that if the atom is moving towards the laser which has a negative detuning of $\delta_L < 0$, the net force operates against the atom's velocity. The atom is damped viscously which gives the optical molasses its name [8]. Consequently, optical molasses can be used for laser cooling of atoms.

Additionally, it can be seen in figure 3 that optical molasses are primarily effective for slow velocities. The velocity range of atoms being addressed by such a cooling laser setup is very limited. To address higher velocities as well without increasing the laser detuning (which would reduce its effect on slow velocities drastically), the energy levels of the atoms are shifted with help of the Zeeman effect (see section 2.1.3). Thus, with the combination of the Doppler shift and the Zeeman shift, a wide range of velocities can be addressed in a laser cooling setup as optical molasses.

In general, the cooling effect of optical molasses is limited to the Doppler cooling temperature $T_D = \hbar\gamma/(2k_B)$, with k_B being the Boltzmann constant [6].

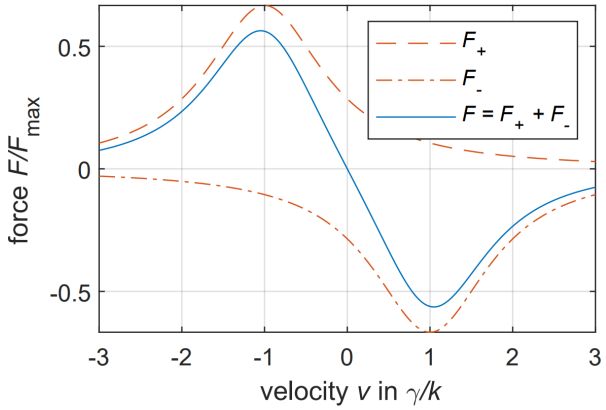

Figure 3: Forces depending on the velocity v of an atom in an one-dimensional optical molasses, with $F_\pm$ as the forces of the single counter-propagating laser beams and their sum F. A linear damping can be observed for small parameter. The saturation parameter is set to $s_0 = 2$. For a laser detuning of $\delta_L = -\gamma$, the maximum force acting on an atom is $F_{max} = \hbar k\gamma/2$. Figure taken from [9].

2.2 Argon level structure

A detailed knowledge about the argon energy spectrum is crucial for a good performance of ArTTA in terms of the cooling and trapping of atoms. The relevant transitions are depicted in figure 4.

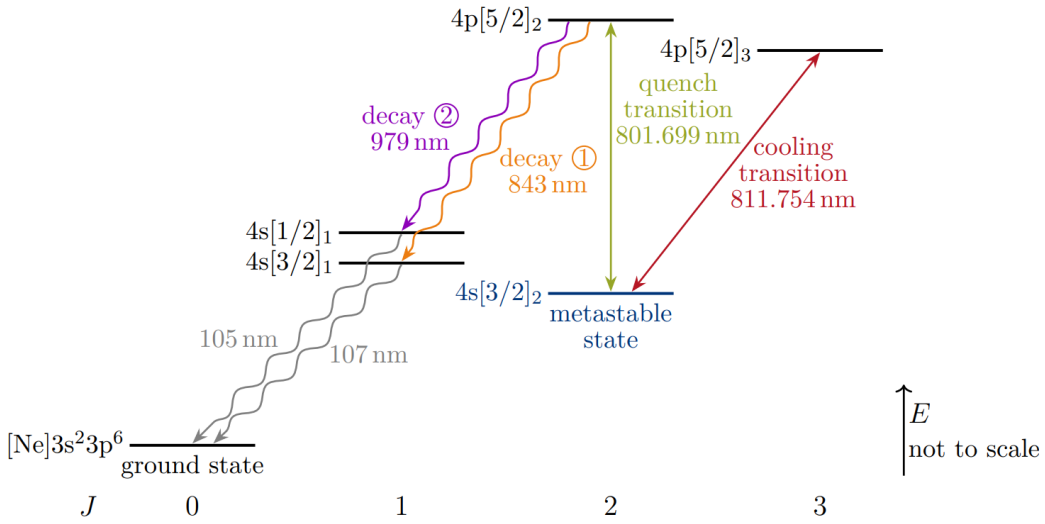

Figure 4: Relevant argon energy spectrum for ArTTA. The explanation of the used notation of the atom states can be found in [8]. The excitation of the atoms from the ground state $3s^2 3p^6$ to the metastable state $4p[3/2]_2$ is carried out by a RF discharge. The metastable state has a closed cooling cycle to $4p[5/2]_3$. The quench transition promotes the atoms to the $4p[5/2]_2$ state, from which they can subsequently decay to the ground state. Figure taken from [8].

As it can be seen, the transition from the ground state $3s^2 3p^6$ to the cooling ground state $4s[3/2]_1$ requires lasers operating in the UV-regime, more precisely at a wavelength of 107nm. Since no conventional lasers and optical components are available in this regime, laser cooling cannot be employed for the ground state of argon.

Instead, using a radio-frequency (RF) discharge, the atom can be exited to the metastable $4p[3/2]_2$ state which has a lifetime of $38^{+8}_{-5} s$ [10]. From there, a closed cooling cycle to the $4p[5/2]_3$ state can be performed using widely available lasers with the operating wavelength $\lambda = 811.754\text{nm}$. The cooling transition is used for the cooling and trapping of atoms. The quench transition from the metastable state to $4p[5/2]_2$ is used for the deexcitation of the atom to the ground state via some interstates. It enables an absolute measurement of the metastable flux due to the emission of precisely one photon at the detection wavelength by each atom undergoing transition to the ground state [8].

2.3 ArTTA-apparatus

In the following, the ArTTA-apparatus is briefly introduced. Its schematic view including the main components is shown in figure 5. A detailed description can be found in [11].

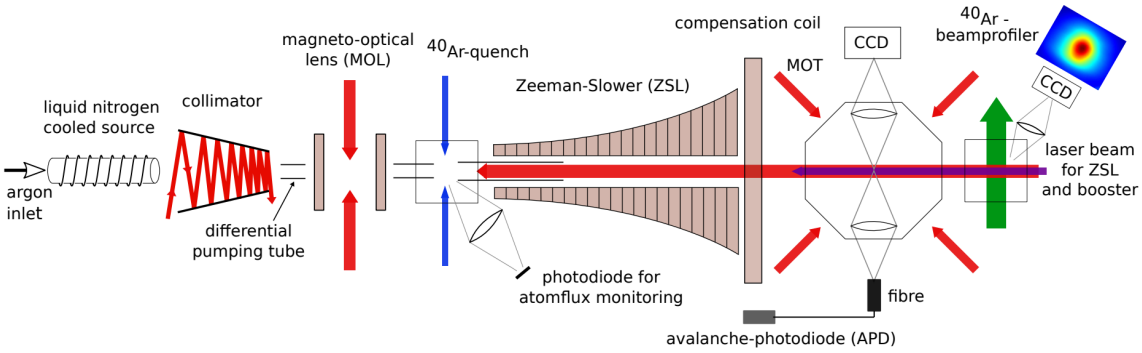

Figure 5: Schematic view of the ArTTA-apparatus. For more details about its components it is referred to [11]. Figure taken from [11].

Radio-frequency discharge source

The argon atoms enter the source chamber through a gas inlet, where the atoms are excited from the ground state into higher energy levels using a RF discharge source. Only the atoms departing the emerging plasma source in the metastable $4p[3/2]_2$ state are of further interest for the experiment (referring to section 2.2). The source is connected to a liquid nitrogen (LN_2) cooling system which reduces the transverse and longitudinal velocity distributions of the emitted atoms. These distributions are further influenced by the spatial mode of the plasma.

Collimator

Since the output of the plasma source is a diverging atomic beam, a collimator is positioned directly behind the source to reduce the transversal velocity of the atoms. The collimation is accomplished via laser cooling in both the horizontal and vertical axis. In each axis, a laser beam undergoes multiple reflections between two tilted mirrors that are facing each other. Between two reflections, the laser crosses the atomic beam and interacts with exactly those atoms that compensate for the Doppler shift induced by the tilt. Consequently, atoms of a wide range of transversal velocities can be addressed and hence cooled.

Magneto-optical lens

Only sufficiently focused atoms arrive at the next chamber where a two-dimensional magneto-optical trap is positioned, also referred to as a magneto-optical lens (MOL). It represents

the second stage for a reduction of the transversal velocities. It consists of two coils in Anti-Helmholtz configuration that induce a splitting of the energy levels according to the Zeeman shift introduced in section 2.1.3. A red-detuned laser beam is installed and crosses the chamber twice with help of retro-reflection. The detuning of the laser in combination with the external magnetic field results in a velocity dependent damping force on the atoms. Taking into account the polarisation of the laser beam, a spatial depending component can be added to the force, as the polarisation or rather the helicity (σ^+ or σ^-) defines the transition which can be excited. For σ^+, the respective state is shifted to a higher energy level, while the shift through σ^- light occurs downwards. The swap in helicity takes place synchronously with the change of direction. All in all, the ensemble of laser detuning, external magnetic field and helicity permits to focus the atoms in respect of their velocities and spatial position. The detailed physics can be found in [12].

^{40}Ar Quench

At this point, the metastable flux comprises ^{39}Ar and ^{40}Ar atoms. Although the lasers of the MOT are configured for ^{39}Ar detection, it is possible that some ^{40}Ar atoms may also interact with the laser beams due to their close resonance frequencies, leading to the scattering of photons. Due to their high abundance, this significantly influences the background noise. Therefore, the ^{40}Ar atoms are deexcited in the quench chamber using the quench transition of 801.699nm, leaving only ^{39}Ar atoms in the metastable state. Since each ^{40}Ar atom emits exactly one photon at a certain wavelength during its decay to the ground state, the detection of this fluorescence signal gives a absolute number of the metastable ^{40}Ar atom flux. By monitoring this so-called quench flux, the performance of the plasma source which excites the argon atoms into the metastable state can be tracked.

Zeeman slower and Booster

So far, the atoms have only undergone transversal cooling, but their longitudinal velocity distribution is still up to several hundred meters per second [9]. In the Zeeman slower (ZSL), the atoms are decelerated down to a velocity of $v \approx 70ms^{-1}$ [8]. The cooling process comprises a detuned laser beam along the atom beam direction and an increasing external magnetic field that cancels the velocity dependent Doppler shift. Because the atoms are still too fast for being captured by the MOT, a second ZSL which is also entitled as Booster further reduces their longitudinal velocity. The final velocity distribution is thus within the required velocity range for being captured by the MOT. A compensation coil separates the ZSL and the MOT chamber. It compensates the high magnetic field at the end of the ZSL, so that it does not effect the trapping process in the MOT.

Magneto-optical trap

In the magneto-optical trap , the metastable ^{39}Ar atoms are cooled in all three dimensions, analogue to the two-dimensional cooling in the MOL (see section 2.3). Once they are trapped,

the fluorescence signal is detected by an avalanche photo diode (APD) which is able to resolve single atom detection. A charge-coupled device (CCD) is used to measure high numbers of trapped atoms. More information can be found in [11].

^{40}Ar beam imaging

In the beam imaging chamber, the transverse profile of the metastable ^{40}Ar flux is resolved. Since the monitored image depends on the performance of the previous system, this tool can be used for real time flux optimization, concerning the alignment of the collimator and MOL.

2.4 Introduction into vacuum technology

In vacuum technology, the magnitude of vacuum is divided in various pressure ranges, as shown in table 1.

Table 1: Pressure ranges in vacuum technology [13]

Low vacuum	300 - 1 mbar
Medium vacuum	1 - 10^-3 mbar
High vacuum	10^-3 - 10^-8 mbar
Ultra-high vacuum	10^-8 - 10^-11 mbar
Extremely high vacuum	$< 10^-11$ mbar

An important parameter for describing vacuum systems is the mean free path

$$\lambda = \frac{1}{n\sigma} \tag{2.9}$$

which represents the average distance that a particle can travel between two successive collisions with other particles. It depends on the particle number density n and the effective cross-sectional area for collision σ. [13]

n is given from the equation of state for ideal gases that says that the particle number density is proportional to the pressure p in a volume.

$$p = n \cdot k_B T \tag{2.10}$$

where k_B is the Boltzmann constant and T the temperature.

The mean free path is useful to describe the type of flow which is characterised by the Knudsen number Kn, the ratio of λ to the flow channel diameter d.

$$Kn = \frac{\lambda}{L} \tag{2.11}$$

The following flow regimes in table 2 are differed by the Knudsen number:

Table 2: Overview of types of flow regimes [13]

	Viscous flow	Knudsen flow	Molecular flow
Knudsen number	$Kn < 0.01$	$0.5 < Kn < 0.5$	$Kn > 0.5$
$p \cdot d$ [mbar cm]	$p \cdot d > 0.6$	$0.6 > p \cdot d > 0.01$	$p \cdot d < 0.01$

While molecular interaction is dominant for viscous flow, these two-body collisions virtually no longer occur in a molecular flow regime. Here, the mean free path is significantly larger than the characteristic length of the system, meaning for example the size of the chamber or of a differential pumping tube (DPT). Instead, collisions between the molecules and the wall dominate the gas behaviour.

As a molecular flow regime prevails in the ArTTA vacuum system, the following formula will only be considered for this regime. A flow is regulated by the conductance of the surrounding apparatus as friction between the gas molecules and the surface of the wall occurs. The conductivity of a pipe or orifice is independent of the prevailing pressure since the molecular interaction is negligible in a molecular flow regime and further dependent of the geometry.

Thus, the orifice conductivity is proportional to the orifice cross section A with

$$C_{or} = A \cdot \frac{\mu}{4}. \tag{2.12}$$

where $\mu = \sqrt{8RT/(\pi M)}$ is the mean thermal velocity, R the gas constant, T the temperature and M the molecular molar mass.

The conductance of a pipe is a function of μ, its diameter d and length l:

$$C_{pipe} = \frac{\mu \pi d^3}{12 \cdot l} \tag{2.13}$$

3 Materials and Methods

3.1 Motivation

Providing an optimized vacuum system is an important factor for approaching a high ^{39}Ar count rate which is crucial for the performance of the ArTTA-apparatus. A high sample throughput increases the absolute number of atoms but at the same time the number of losses due to collision with the background gas. [1] By creating a sufficiently high vacuum these losses can be reduced [15]. A scattered atom is considered lost as it falls from its metastable state back to the ground state and therefore, cannot get detected in the MOT anymore. The significance of these losses is pointed out in [11], where it is said that around 30% of metastable atoms are lost due to collisions with the background gas and hence do not contribute to the count rate.

In figure 6, a model of the ArTTA vacuum system and a corresponding horizontal cross section of the simulated pressure is depicted [11]. Since the model was calculated, some small changes to the system were implemented which are hence not depicted in the figure. However, the further qualitative analysis equally applies for the changed system. Marked in red, the occurrences of problematic high pressure areas are visible in the source chamber, in the ZSL as well as in the DPTs. According to eq. 2.13, their small diameters induce a low conductance inside of the tubes and hence, higher pressure builds up in there leading to more collisions and thus losses.

Figure 7 shows the simulated pressure profile along the beam axis of the ArTTA system, whereby only the blue line from figure 6 corresponding to the current system is considered for this thesis. In the 1$^{\text{st}}$ and 3$^{\text{rd}}$ DPT, the pressure has a huge increase and causes a high loss rate due to collisions with the background gas. The remaining metastable atoms in the vacuum system are depicted in the lower graph in figure 7. According to [11], already 15% of all metastable atoms are deexcited again at the end of the 1$^{\text{st}}$ DPT.

The source emits atoms in a divergent beam. The 1$^{\text{st}}$ DPT shields the atoms with high transversal velocities to minimize the background pressure in the further vacuum system. At the same time, a DPT is counterproductive in terms of working with metastable atoms because the high pressure inside the DPT causes a high loss rate which derives from the extent of random scattering in small tubes. If a diverging atom hits the wall, the scattering from the surface has no favoured direction, meaning it is unrelated to its direction of incidence.

[1] Even though a molecular flow regime prevails in the machine [2], collisions deexciting metastable atoms occur. This probably originates from the following two facts: The total collision cross section for metastable argon atoms is greater than for unexcited argon atoms [14]. A calculation follows in the appendix A.2. And, the atoms in the atomic beam have a relative velocity to the background gas. This increases the probability for collisions.

[2] $(p \cdot d)_{\text{ArTTA}} \lesssim 10^{-4} \cdot 10^{0} = 0.0001$, whereby a molecular flow is defined by $p \cdot d < 0.01$ (see table 2).

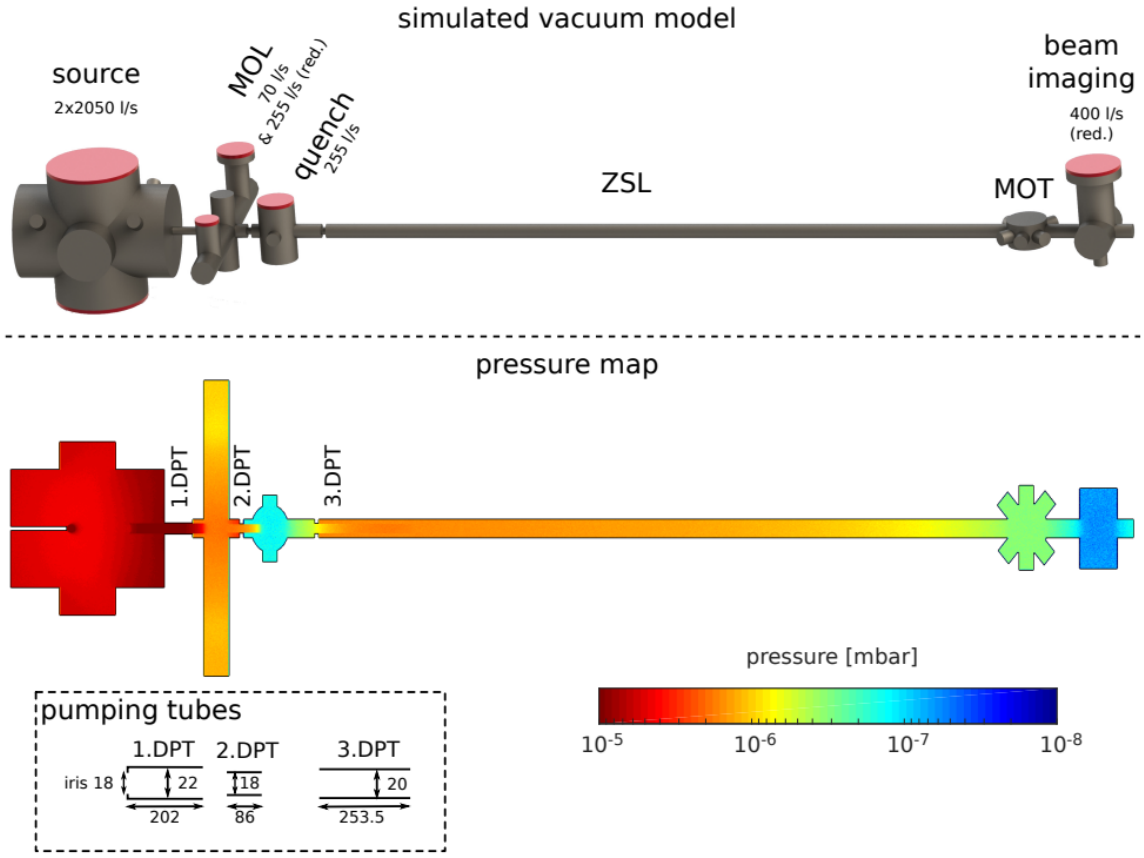

Figure 6: **Upper figure:** Simulated vacuum model of the ArTTA system. The vacuum pumps are marked by the red faces, with corresponding pumping speeds indicated above.
Lower figure: Simulated pressure map of the ArTTA system. The occurrence of high pressure ares in the source chamber, in the ZSL and in the DPTs are clearly visible. The dimensions of the DPTs are shown in the small inset.
Figure taken from [11].

Instead, it follows a cosine distribution [16]. Therefore, the atoms that scatter inside the tube with the wall stay there for a while until they find their way out again. That is to say, pumping in high vacuum regimes is not about molecules getting drawn away by a pump like in the laminar flow case but rather about a probability of an atom to arrive at the entrance of a pump by chance due to their thermal motion [17].

In [11], the vacuum system of the ArTTA-apparatus was investigated in detail, with the following outlook given: 'the biggest potential for further improvements of the vacuum system lies in rapid pressure decrease directly behind the source, for example with help of an iris [...]' ([11], p. 42). The idea is that by removing the DPT and installing an iris at the exit of the source chamber instead, diverging atoms are still geometrically restricted and remain in the source chamber but at the same time, the occurrence of a pressure peak in the 1st

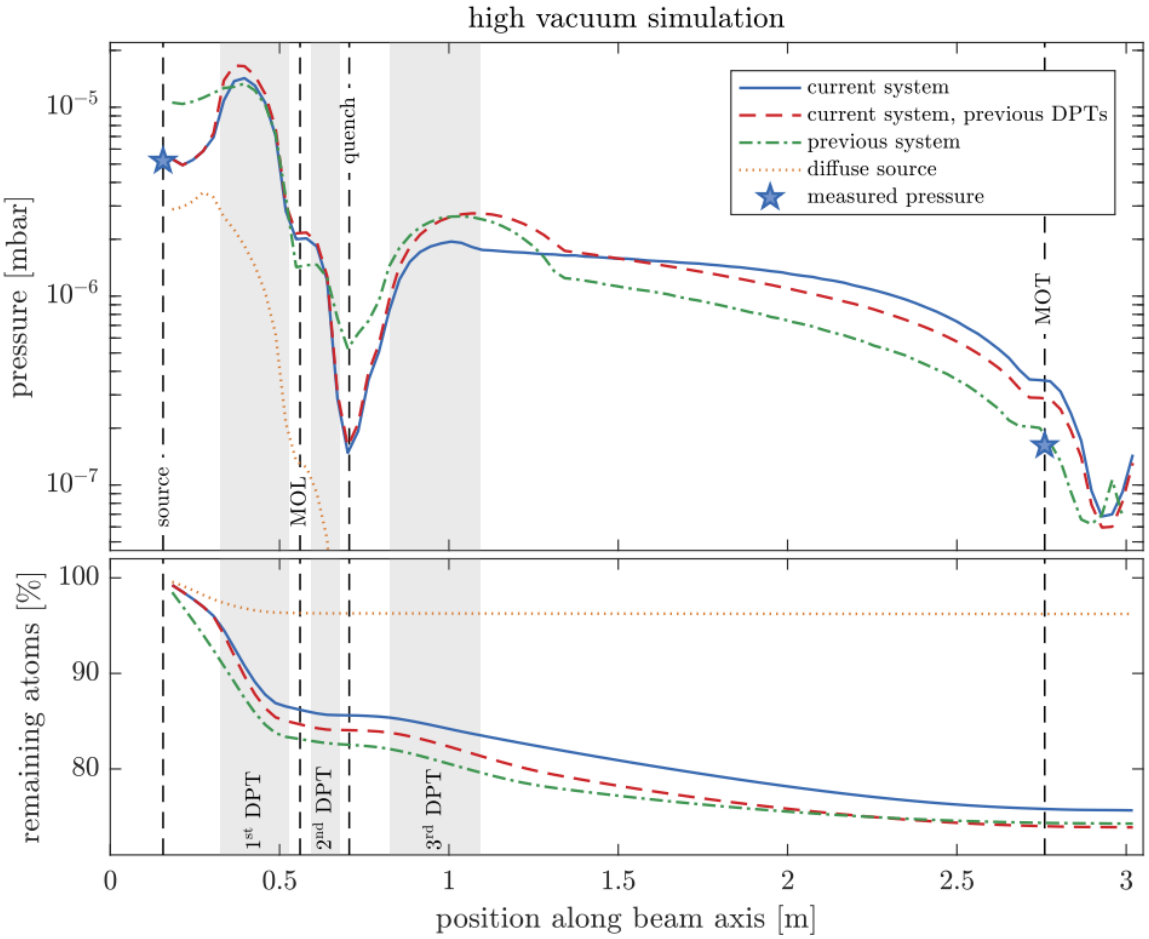

Figure 7: **Upper plot:** Simulated pressure profile along the beam axis of the vacuum system in ArTTA. Only the blue line depicting the current system is considered for the motivation of this thesis. Hugh increases in the pressure are visible in the 1^{st} and 3^{rd} DPT.
Lower plot: Remaining atoms in the vacuum system along the beam axis. Losses are caused by collisions of metastable atoms with the background gas. Figure taken from [11].

DPT is suppressed. A larger diameter of the connecting tube improves the conductance and increases the probability that a scattered atom find its way out again. This thesis investigates the given outlook. The hypothesis is that for any setup the flux of metastable atoms will rise with increasing pressures. It is furthermore assumed that for high pressures, the flux eventually declines due to scattering with the background gas, resulting in losses of the metastable atom flux.

3.2 Realisation

For the investigation of the outlook named above, two irises of diameters $d_1 = 22\,\text{mm}$ and $d_2 = 30\,\text{mm}$ were designed to be attached to the back wall of the source chamber. The exact position is indicated in figure 8. It is assumed that for a direct attachment of the iris to the back wall, the atoms would concentrate directly behind the iris and form a high scattering area. If so, mounting the iris with an offset to the chamber wall would solve this problem as atoms can exit the tube through the full diameter. The offset denotes a displacement of the iris from the back wall, so that a certain distance is left in between. Both irises and the optional offset setup are shown in figure 9.

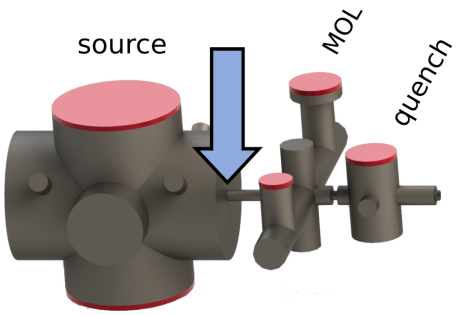

Figure 8: Demonstration of the positioning of the iris configurations at the exit of the source chamber in the ArTTA-apparatus, indicated with a blue arrow. Figure adapted from [11].

In favour of completeness and comparability with the previous vacuum system, a measurement cycle with a DPT and one without any restrictions in diameter is executed as well. These are the resulting six configurations that are investigated in the following:

1. Differential pumping tube $d_{\text{dif}} = 22\,\text{mm}$, $l = 173\,\text{mm}$ (original setup)
2. No iris, no DPT
3. Small iris without offset, $d_1 = 22\,\text{mm}$, $x = 0\,\text{mm}$
4. Small iris with offset, $d_1 = 22\,\text{mm}$, $x = 37\,\text{mm}$
5. Big iris without offset, $d_2 = 30\,\text{mm}$, $x = 0\,\text{mm}$
6. Big iris with offset, $d_2 = 30\,\text{mm}$, $x = 37\,\text{mm}$

d is the respective diameter, l the length of the differential pumping tube and x the offset between iris and the back wall of the source chamber. Figure 10 depicts the configurations No. 1, No. 3 and No. 4 installed in the source chamber.

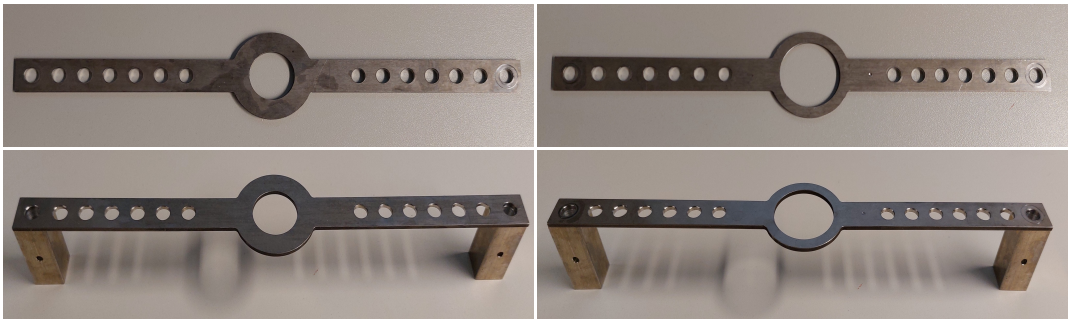

Figure 9: Newly designed irises for vacuum measurements. Iris with small diameter ($d_1 = 22\,\text{mm}$) on the left and with big diameter ($d_2 = 30\,\text{mm}$) on the right. The lower photos show the same iris from above but this time mounted on distance pieces.

To quantify the effect of scattering of each configuration, the respective atom fluxes [3] have to be measured. It is plausible to use the already existing setup for measurements of the metastable argon flux in the quench chamber, which is also named quench flux (see section 2.3). Irises with a bigger diameter permit a higher throughput of atoms and thus induce a higher quench flux. Since only the intensity of the atom beam and not the absolute number depending on the iris size should be measured, an additional iris of diameter $d = 18\,\mathrm{mm}$ is mounted at the entrance of the quench chamber. It is aimed to cut off the atom flux in diameter for all configurations, so that only the intensity of the atomic beam is measured in

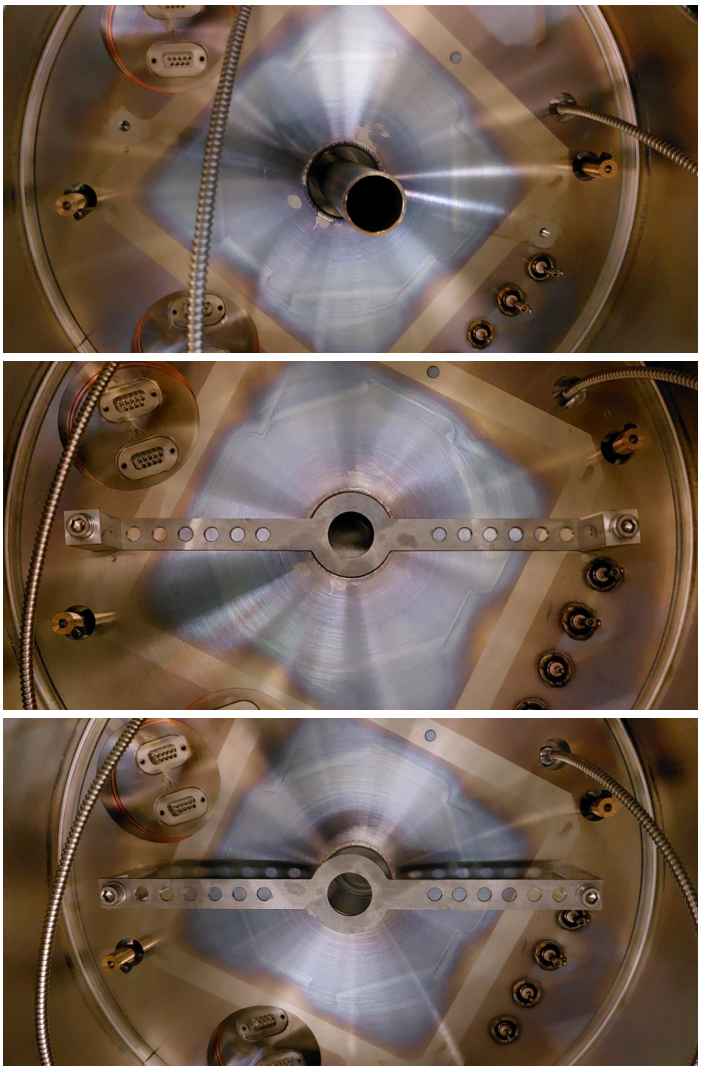

Figure 10: Different configurations installed at the end of the source chamber: differential pumping tube, small iris without offset, small iris with offset (from top to bottom).

[3] Meaning the flux of metastable atoms.

the quench chamber, since the interest is in resolving the scattering. As the scattering rate is also dependent on the current pressure, each flux measurement will be done for various pressures. The pressure can be varied by changing the amount of argon gas that goes into the system.

To provide that the measurements of the quench flux were taken under the same conditions, it is necessary to have a simultaneous measurement of the atom flux before it reaches the exit of the source chamber. This control measurement should be the same for all iris configurations as any changes just take place in the further apparatus. The importance of this second setup especially lies in the inconsistency of the performance of the plasma source. The source can burn in different modes that provides different atom fluxes and hence different quench signals. This correlation was further investigated in [18]. In other words, controlling the atom flux in the source chamber assures that the quench data can be normalised for all setups.

The control of the initial atom flux happens through an absorption measurement where a laser with the frequency of the cooling transition of ^{40}Ar $\nu = 811.754$nm (see section 2.2) goes through the source chamber, perpendicular to the atomic beam. The power of the laser is measured before and after the chamber. The metastable atoms interact with the laser light, meaning that they absorb and emit photons various times. The emitted photons do not necessarily have the same direction as the absorbed photons as the spontaneous emission is the dominant emission process. So, whenever the beam of metastable atoms crosses the laser, there is a drop in the laser power after the chamber due to absorption. This drop is proportional to the number of metastable atoms in the atomic beam which in turn depends on the mode of the source.

While the quench flux measures the absolute flux of metastable argon, the absorption setup measures a relative signal which suffices to normalise the measurements.

3.3 Experimental setup

The implementation in the ArTTA system is described in the following, including a detailed depiction of the optomechanical setup for the absorption measurements. Consequently, further settings that had to be considered during the installation of the absorption setup are listed.

3.3.1 Optomechanical setup

A schematic drawing of the optomechanical setup of the cooling laser is shown in figure 11.

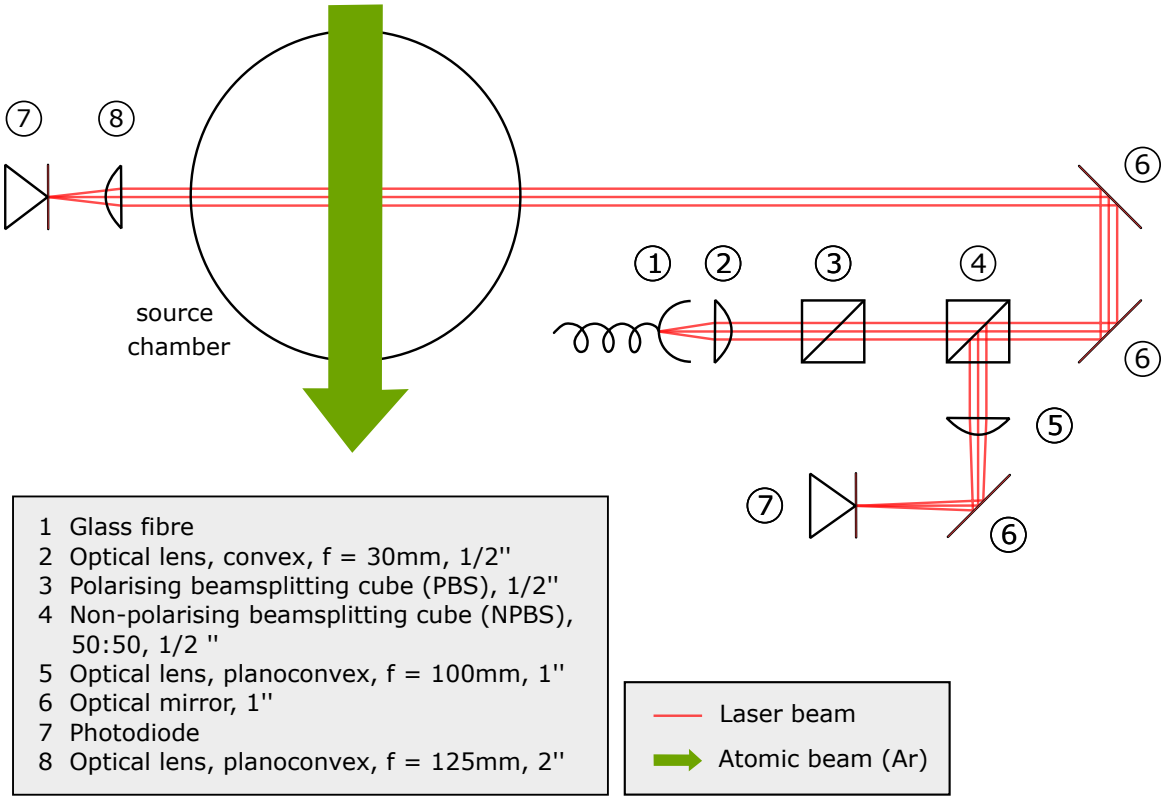

Figure 11: Schematic drawing of the absorption setup. The cooling laser crosses the atomic beam perpendicularly in the source chamber. As long as argon atoms are within the laser beam, they absorb and emit photons while getting excited and deexcited spontaneously. The power of the laser is monitored by a photodiode before and after the source chamber to measure the generated absorption signal.

A glass fibre leads the laser light of cooling frequency from the optical table to the experiment (see figure 12, left), where the fibre outlet is mounted on a rotation mount. A convex lens with a focal length of $f = 30\,\mathrm{mm}$ collimates the outcoming laser light. The lens is cemented achromatic doublet whose high quality is necessary to prevent the formation of

interference rings within the relevant distance [19]. The collimated laser beam has a diameter of $d = 5.85\,\text{mm}$. However, the visible diameter just comprises $d \approx 3\,\text{mm}$ due to the fact that the following measurements will be performed with a very low laser intensity. More on this in section 3.3.2.

The glass fibres in the laboratory are not perfectly polarisation-maintaining. Instead, the polarisation is slightly sensitive to temperature changes. Therefore, a cleaning cube is installed after the fibre to filter out the non-linear part [4]. The maximal transmittance of the laser light through the polarising beamsplitting cube (PBS) can be found by turning the rotation mount. However, the cleaning cube is not mandatory in this setup since the other optical elements might just have a minimal dependence on the polarisation of the incident light [20].

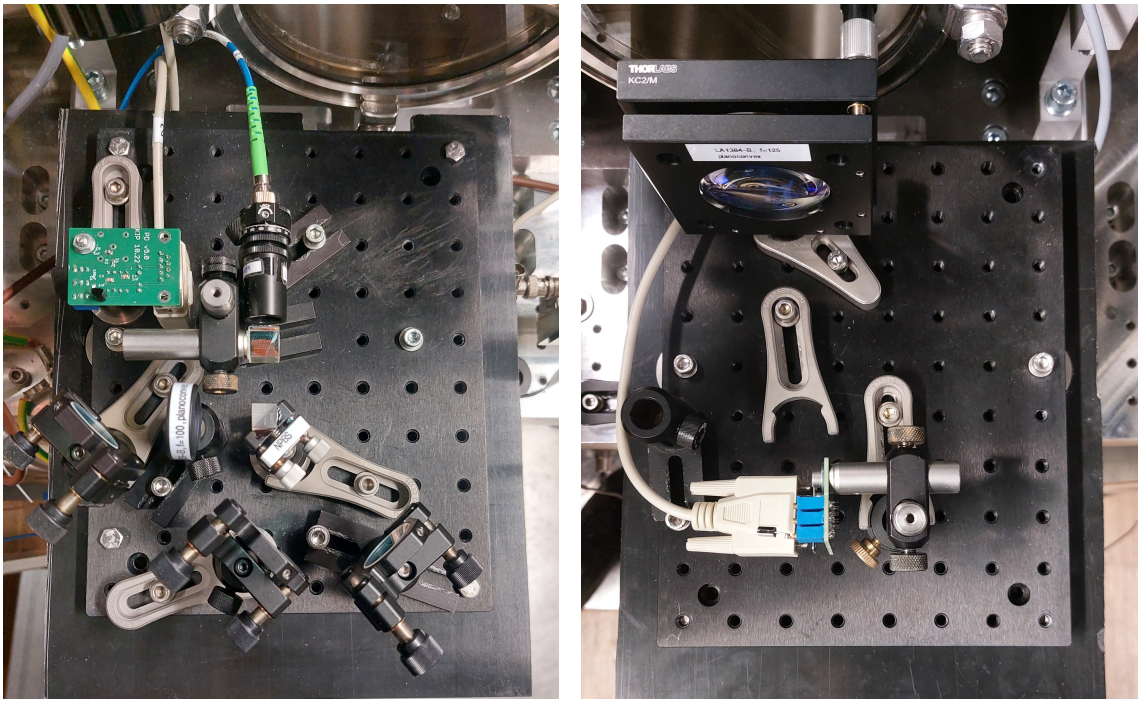

Figure 12: Optomechanical setup of the absorption measurement before the source chamber (left) and after the source chamber (right): On the left, the blue fibre leads the cooling laser from the optical table to the experiment. 50% of the beam is transferred onto the first photodiode for power controlling (black square on the green printed circuit board). The other 50% of the laser is guided into the source chamber which is at the top of the photo. On the right, the laser exits the source chamber at the top and is focused onto the second photodiode to monitor the remaining laser power.

[4] The light that comes out of the fibre is linearly polarised.

Next, the beam goes through a non-polarising beamsplitting cube (NPBS) that provides a 50:50 beamsplitting ratio. The reflected part of the beam serves for power controlling. A planoconvex lens with $f = 100$ focuses the beam on a photodiode, whereby there is a mirror placed in-between which simplifies the adjustment. The photodiode translates the incident photons into a current which is translated into a voltage afterwards by a transimpedance amplifier with adjustable resistances. The signal is subsequently read out by an arduino. This voltage is monitored during the measurement to control the laser power.

The other 50% of the original beam proceed into the experiment. To assure that the laser beam crosses the centre of the atomic beam in the source chamber accurately, having four degrees of freedom in the positioning of the laser beam is required: two for the spatial displacement of the beam and two for the adjustment of the angle. This can be accomplished by setting up two mirrors in a row.

After crossing the source chamber perpendicularly, the laser beam is focused by a planoconvex lens with $f = 125\,\text{mm}$ onto a second photodiode through which the laser power is monitored similarly to the first photodiode (see 12, right). If the source is turned off, the laser crosses the source chamber without any interaction. Switching on the source causes a dip in the signal of the laser power whose depth is proportional to the flux of metastable atoms. These dips are entitled as absorption signal in the following.

3.3.2 Further settings

Alignment and placement of the laser beam:
As already said, the cooling laser addresses the metastable atoms. This means that it is crucial for the absorption measurements that the laser beam crosses the atomic beam at a point where most of the atoms are already excited to the metastable state. In [18], the excitation distribution of the argon atoms was measured for distances up to $d \simeq 23\,\text{mm}$ to the source. It was found that a non-negligible part of the argon atoms are exited outside of the source tube where the plasma burns, whereas this part decreases with increasing distance to the source. Moreover, it was shown that these distributions change with the respective plasma mode and pressure. However, for $d \simeq 23\,\text{mm}$, at least 80% of the atoms are excited to the metastable state for all relevant plasma and pressure configurations.

In respect of that work, the absorption laser in this experiment is placed with maximal possible distance to the source, which are $d \approx 43\,\text{mm}$. The distance is limited by the size and position of the side windows in the vacuum chamber through which the laser enters and exits. All in all, it can be expected that in a distance of $d \approx 43\,\text{mm}$, the percentage of excited atoms is sufficiently high for the planned measurements.

Furthermore, in view of the complete ArTTA-apparatus, it has to be considered that only metastable atoms without significant transversal velocity will arrive at the end of the appa-

ratus and hence contribute to the count rate in the MOT. To address only these atoms with the cooling laser within the framework of the absorption measurement, the cooling laser has to be perpendicular to the atomic beam and must go right through its centre.

The atoms that are ultimately addressed can be spotted as a luminous purple spot in the path of the atomic beam due to their fluorescence, which can also be seen in figure 13. That means that if this spot is right in the centre in front of the plasma source, the absorption laser is well aligned. Consequently, the alignment can be done just visually. When aligning the vertical axis, any deviation from the central position is visible as an offset in upper or lower direction and can be corrected easily. In contrast, aligning the horizontal axis, thus changing the angle between both beams, deviates the purple spot towards or away from the incident laser. Any deviation in angle leads to a small frequency detuning due to the Doppler shift (see section 2.1.2) for which reason only atoms with a correspondent transversal velocity would be cooled. So, regulating the location of the fluorescing atoms in the centre of the atomic beam ensures that only metastable atoms without transversal velocity are addressed by the cooling laser and hence perceived by the absorption signal.

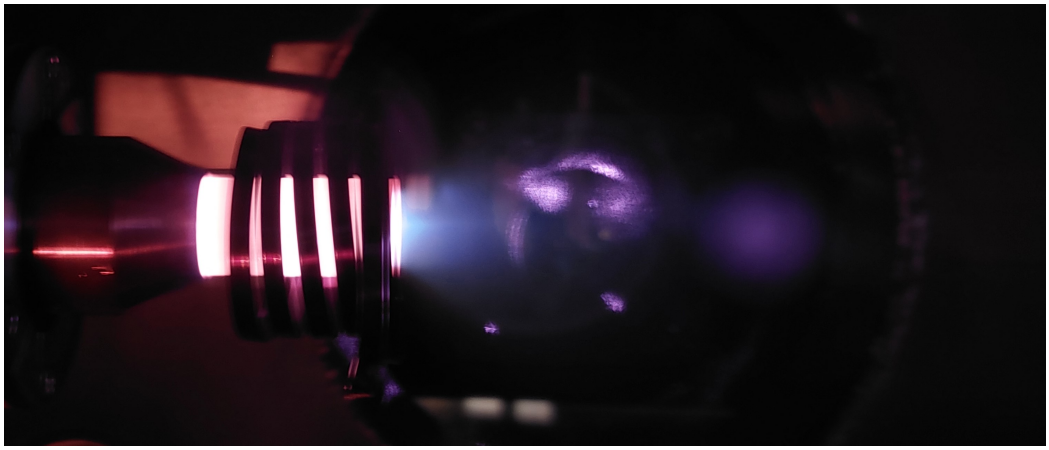

Figure 13: Fluorescence of the cooled atoms in the path of the atomic beam. The plasma source on the left emits metastable argon atoms. The atomic beam which is not directly visible goes from left to right. The cooling laser comes out of the image plane. At the intersection point the fluorescence of the cooled atoms is visible as a luminous purple spot. The central positioning of the fluorescing atoms in the atomic beam marks the good perpendicular alignment of the two beams.

Regulating the laser power:
Every atom absorbs just a limited number of photons while crossing the laser beam that is independent of the power of that beam, as long as it is in saturation. This means that with a low laser power a higher relative absorption signal can be reached and thereby, potential fluctuations in the signal will have a relatively lower effect. Concluding, the laser power was set to be in the order of some micro watts.

A transimpedance amplifier with adjustable resistances translates the incoming current I from the photodiode to a voltage U, according to Ohm's law

$$R = U \cdot I. \tag{3.1}$$

To receive a well resolvable voltage, the resistances mounted on the transimpedance amplifier were tuned to their maximal value, $R \simeq 555k\Omega$.

Another aspect is that due to the low laser power, having any stray light is fatal. Therefore, two black boxes were designed and placed around the two setups. In the monitored absorption signal it was clearly visible that this step was crucial for the quality of the measurement.

Setup of the ArTTA-apparatus:
It has to be said that the present ArTTA apparatus deviates from the introduced apparatus in sec. 2.3. The current apparatus lacks the collimator as well as the MOL optics, and it ends with the quench chamber. A corrugated hose connected to a turbomolecular pump is mounted instead of the usual ZSL, so that the pressure profile in the standing vacuum system equals the one of the complete apparatus.

3.4 Measuring procedure

This section depicts the measuring procedure, including the preparation and the measuring process itself. A full procedure of a measurement cycle includes a former check-up of all starting parameters, so that each measurement starts under identical initial conditions to guarantee reproducibility and hence comparability of the different cycles.

3.4.1 Preparation

For controlling the starting parameters, it is very important to check the laser power of the cooling laser which can be done by holding a power meter into the beam after the source chamber. It is aligned to a very low value of $P \simeq 3.7\mu$W, according to the considerations in section 3.3.2.

Furthermore, the initial pressures in the source chamber, MOL chamber and quench chamber are read off the respective pressure gauges. This was done before any argon gas was let into the system. By reading off the pressures, the quality of the vacuum is checked which was necessary for the following reason. Between two measurement cycles, the vacuum system had to be opened to change the iris configuration. Over night, the apparatus was evacuated again, so that each day a new measurement could start. These initial pressures were controlled to guarantee the comparability of the different measurements. Subsequently, the pressure

gauges in the MOL chamber and in the quench chamber are turned off, because they generate a blinking light while turned on which creates additional noise in the monitored data.

3.4.2 Measurement

For each iris configuration in 3.2, one measurement cycle was carried out. During one cycle, the following parameters were monitored:

$\mathbf{p}_s$**:**	pressure in the source chamber
$\mathbf{P}_{\text{source}}$**:**	source power
$\mathbf{P}_{\text{abs,pre}}$**:**	laser power of the absorption laser, measured before the source chamber (for power controlling)
$\mathbf{P}_{\text{abs,post}}$**:**	laser power of the absorption laser, measured behind the source chamber (for measuring the absorption signal)
$\mathbf{P}_{\text{qu}}$**:**	laser power of the quench laser (for power controlling)
Q:	quench flux

The pressure range goes from $6{\cdot}10^{-6}$ mbar to $1{\cdot}10^{-5}$ mbar in steps of $1{\cdot}10^{-6}$ mbar, continuing in steps of $0.25 \cdot 10^{-5}$ mbar up to $3.5 \cdot 10^{-5}$ mbar. For each pressure value, the absorption and quench signal are measured twice.

For starting a measurement cycle, the monitoring on the computer of the listed parameters is actuated once and keeps running for all data points taken. Starting with the source turned off, the following quick method is applied:

1. Regulate the pressure of the source chamber to the right value.
2. Turn on the source.
3. If necessary, change the settings on the network monitoring circuit slightly or wait until the correct plasma mode is burning.
4. Start the timer for 1min.
5. Check constantly if all parameters are performing well.
6. Turn off the source when the timer stops.
7. Repeat for each pressure value.

The setting of the plasma mode can primarily be done visually. Additionally, the mode itself and its stability should be verified by checking $P_{\text{abs,pre}}$, P_{qu} and the source power. If both can not be guaranteed, that data point has to be repeated. Turning off the source each time between two data points would not be necessary if there was no longtime drift of $P_{\text{abs,post}}$. By turning it off it, the final absorption signal can be corrected for this longtime drift in the evaluation. If all data points of a measurement cycle are measured successfully, the vacuum is shut down to change the iris for the next measurement cycle which can be executed the next day when the vacuum is build up again.

4 Results

First, a model is developed to quantify losses in the atom flux as a function of the source pressure for a fixed but arbitrary position. In the following, the monitored absorption and quench signal are plotted against the pressure, with the introduced model fitted to the data points. The data for the six distinct iris configurations are furthermore described and discussed.

4.1 Model

In the work of [11], a quantification of the losses of metastable atoms due to collisions with the background gas (see section 3.1) is given. The respective formula provides the number of metastable atoms $I(z)$ that remains at position z along the beam axis as a function of the initial number I_0.

$$I(z) = I_0 \exp\left(-\int_0^z \frac{1}{\lambda(z')}\, dz'\right) \tag{4.1}$$

In consideration of the varying vacuum conditions areas along the beam axis, it is integrated over the mean free path λ of the atoms, also given by $\lambda(z) = {}^1/_{\sigma n(z)}$. Here, the particle density $n(z) = {}^{p(z)}/_{k_B T_{bg}}$ is a function of the pressure profile $p(z)$ which is of further interest for this thesis. k_B and T_{bg} denote the Boltzmann constant and the temperature of the background gas. σ defines the cross section for collisions between metastable argon atoms and the background, meaning unexcited argon atoms.

This formula is a physical application of the Beer-Lambert law (see [21]) in terms of losses through collisions.

4.2 Data evaluation

For the the evaluation of the measurement data, first, the monitored absorption laser power behind the source chamber is corrected for potential longtime drifts. It is possible to describe this drift with a polynomial function which is thus subtracted from the actual absorption signal. Next, for each pressure value measured for 1min, the mean of the respective absorption depth and the quench flux is formed, so that for each signal only one data point describes one pressure point taken. It is important to note that the pressure gauges in the machine display the pressure for N_2 gas by default. To obtain the effective pressure for argon gas, the indicated pressures must be multiplied by a factor C. For pressure regimes below 10^{-3} mbar, this factor is defined to be $C = 0.8$, given by the production company itself [22].

For evaluating the data, first, both the absorption and quench signal are fitted against the pressure respectively for each iris configuration. The data can be seen in figure 14 whereby

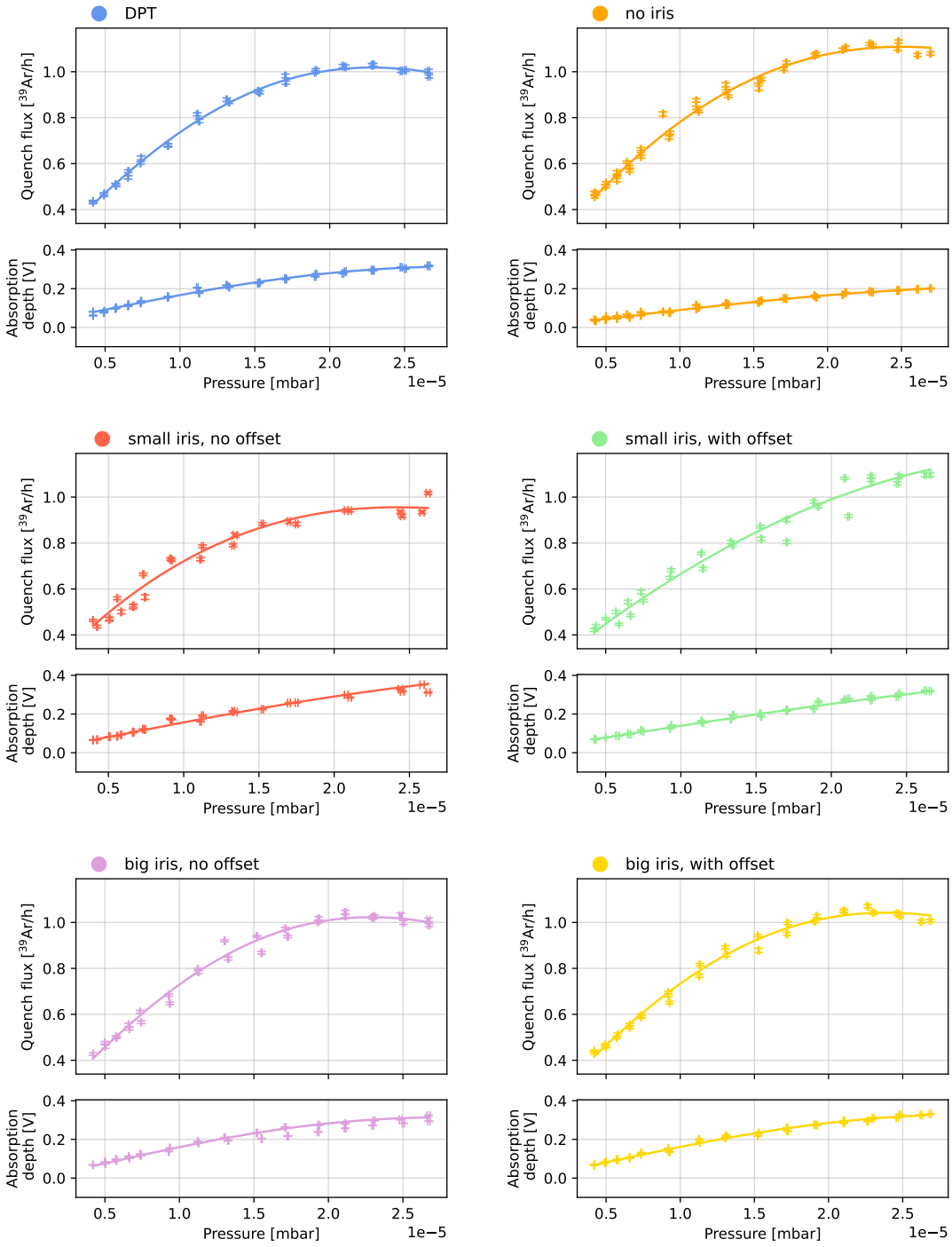

Figure 14: Pressure dependency of the absorption and quench signal individually plotted for all six iris configurations. The lower curves describes the initial atom flux, given by the absorption depth. The upper curve gives the respective quench flux. It shows a linear dependency for lower pressures with a flattening for higher pressures.

the fits are explained in the subsequent paragraph. The errorbars originate from systematic errors introduced during data acquisition and statistical errors due to averaging over a 1min measurement interval. These uncertainties are combined using standard Gaussian error propagation [23]. For simplicity, they are not further illustrated in any further plots, but are still taken into account for the calculations. Before the measurements, it was assumed that for an increase in pressure the atom flux rises as well, which can be verified when looking at the plots. For a more detailed description, regarding the data points representing the absorption depth, in all six cases for lower pressures a linear trend is visible that slightly flattens out for higher pressures. A similar behaviour can be found for the quench flux which first, increases linearly with the pressure. Starting at $\sim 1.0 \cdot 10^{-5}\,\mathrm{mbar}$, the straight line flattens out and for almost every configuration, even reaches a negative slope for pressures above $\sim 2.3 \cdot 10^{-5}\,\mathrm{mbar}$. That means that a higher atom flux for increasing pressures is not always true. The assumption is that scattering becomes dominant and leads to flux reduction due to losses through collisions of metastable atoms with background gas. Investigating the flattening of the curves is key within the framework of this thesis.

In the next step, the measured data was aimed to be described by a physical model to compare the fit parameters afterwards. The measured absorption depth represents the initial atom flux, denoted by I_0. Due to the limited understanding of the plasma source, the absorption depth was approximated by $I_0^{\mathrm{abs}}(p) = A\,p\,\exp\left(-B\,p^2\right) + C$, where A, B and C denote fit parameters. The idea was to combine a linear term, representing the linear trend of the absorption signal for lower pressures, with an exponential term that describes the flattening for higher pressures. The fit function seems to describe the measured data pretty closely. However, finding a reliable physical model is therefore an important outlook given by this thesis.

The quench flux was monitored to resolve scattering occurring between source chamber and MOL chamber. Due to considerations in section 3.1, it was assumed that losses of metastable atoms due to collisions with the background gas affects the curve of the quench signal. A quantification of these losses is given by eq. 4.1, which consequently was used as model for fitting along the quench data points. One assumption that had to be made is the approximation of the pressure profile as $p(z) = p(p_0, z) = p^*(z) + p_0$, meaning that the measured source pressure p_0 only incorporates as an offset. The initial metastable flux was describes to be proportional to the absorption signal. The resulting model is given by

$$I(p) = a\,I_0^{\mathrm{abs}}(p)\,\exp\left(-b\,p\right) + c \tag{4.2}$$

whereby a, b and c are fit parameters, expected to describe the overall atom flux, the scattering rate and the offset of the experimentally determined data. A detailed derivation of this formula can be found in the appendix A.1. The introduced model was applied to the data points in figure 14 and captures the observed data quite accurately, as evidenced by the reduced chi-square values ranging from 4 to 44. Only for the orange curve (no iris) and the yellow curve (big iris, with offset), the model fails to fully capture the decline in the quench flux at high pressures.

4.3 Discussion

For better comparison, all six configurations are conjoint in figure 15. The absorption signals agree very well with each other which implies that the data was monitored under comparable conditions. Only the orange plot, representing the measurement without iris, falls out of line. It depicts a lower atom flux which could originate from a different spatial plasma mode, but in the end it can not be well-justified. Unintuitively, the corresponding quench flux is even higher than the others which however in general concurs with the fact that greater diameters permit more atoms to pass through and arrive at the quench chamber. It should be noted that differences in the overall atom flux between the different configurations were tried to be avoided by installing an 18 mm-iris in the quench chamber. The atom flux, monitored by the quench flux measurement, is hence equally cut off in diameter for all configurations. In other words, the iris was indented to only monitor changes in the intensity of the atomic beam, giving conclusions about the scattering rate. But looking at the data for no iris, the larger initial slope for lower pressures indicates that there still was a larger throughput, despite the compensation with the additional 18 mm-iris in the quench chamber. The total atom flux is defined by the fit parameter a.

Next, comparing the quench fluxes, the green curve for the setup with a small iris with offset stands out. While the others flatten out enormously and even decline for higher pressures, the green curve rises steadily. The comparably low slope in the beginning implies that there are less atoms passing through the iris in the first place, but due to an apparent low loss rate the atom flux for higher pressures outnumbers the others. However, this result has to be taken with caution since the green slope clearly differs from the others and in addition, has the highest variance in its data points, as it can be seen in figure 14. Therefore, it would be very interesting to replicate this measurement, to test its reliability.

Since fit parameter b describes the scattering rate, which is from great interest for this thesis, the losses as a function of the pressure are displayed in figure 16. The corresponding b-values for all six configurations are denoted in a small inset, comprising relative errors under 6%. According to the plot, the small iris with offset has the lowest scattering rate with $b = (1.32 \pm 0.07) \cdot 10^4\,\mathrm{mbar}^{-1}$. The smaller the b-parameter, the less atoms got lost between the positions of the absorption and quench measurement and hence the less scattering happened. Considering the setups of the big iris without offset, the big iris with offset and the DPT, their loss rates lay very close to each other, noting $b_{\mathrm{big,no}} = (1.67 \pm 0.05) \cdot 10^4\,\mathrm{mbar}^{-1}$, $b_{\mathrm{big,off}} = (1.78 \pm 0.04) \cdot 10^4\,\mathrm{mbar}^{-1}$ and $b_{\mathrm{dif}} = 1.77 \cdot 10^4\,\mathrm{mbar}^{-1}$. The big iris setups with and without offset were expected to have quite similar scattering rates, since they only differ in their offset. It was assumed that an offset would induce a lower pressure in the tube and therefore less scattering with background gas since the particles find their way out of the tube easier (see section 3.1). However, this assumption could not be proven by the measurements.

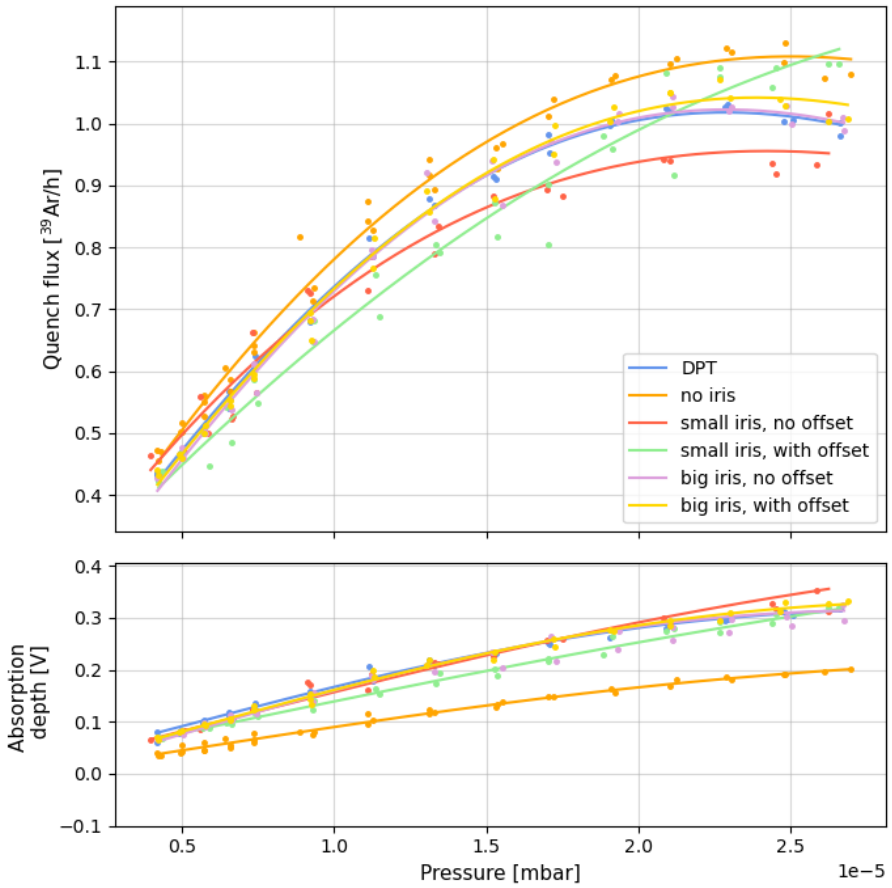

Figure 15: Absorption and quench signal as a function of the pressure for all iris setups. **Lower subplot:** The absorption depths representing the initial atom flux agree very well with each other, besides the orange curve corresponding to the configuration without iris which shows a significantly lower atom flux. **Upper subplot:** The quench fluxes show a flattening for higher pressures which is assumed to originate from losses through collisions. The green curve (small iris, with offset) stands out with its steep slope for higher pressures.

It was further predicted that for the DPT setup, the scattering and hence the loss rate would be remarkably high due to its small diameter. This could not be resolved in the measurements, as the corresponding curve resembles the plots for the big iris setups. Furthermore, inferring from the high overall flux for the no iris setup (referring to figure 15), it could be that the overall atom flux affects the measured data in spite of the installed quench iris. Thus, the flux through the DPT was expected to be comparably lower than the others which is not the case. The setup without iris shows a loss rate of $b = (2.30 \pm 0.04) \cdot 10^4\,\mathrm{mbar}^{-1}$. Possibly, it has the second highest loss rate due to its steep initial slope, meaning that a high b-parameter is needed to flatten out the curve. With $b = (2.92 \pm 0.05) \cdot 10^4\,\mathrm{mbar}^{-1}$, the highest loss rate is depicted for the small iris without an offset. It is not intuitive that both small iris setups denote the best and the worst setup since the missing offset is only a small change in the configuration. Amongst others, this emphasises the question about the exceptional slope of the quench flux, corresponding to the small iris with offset. An additional source

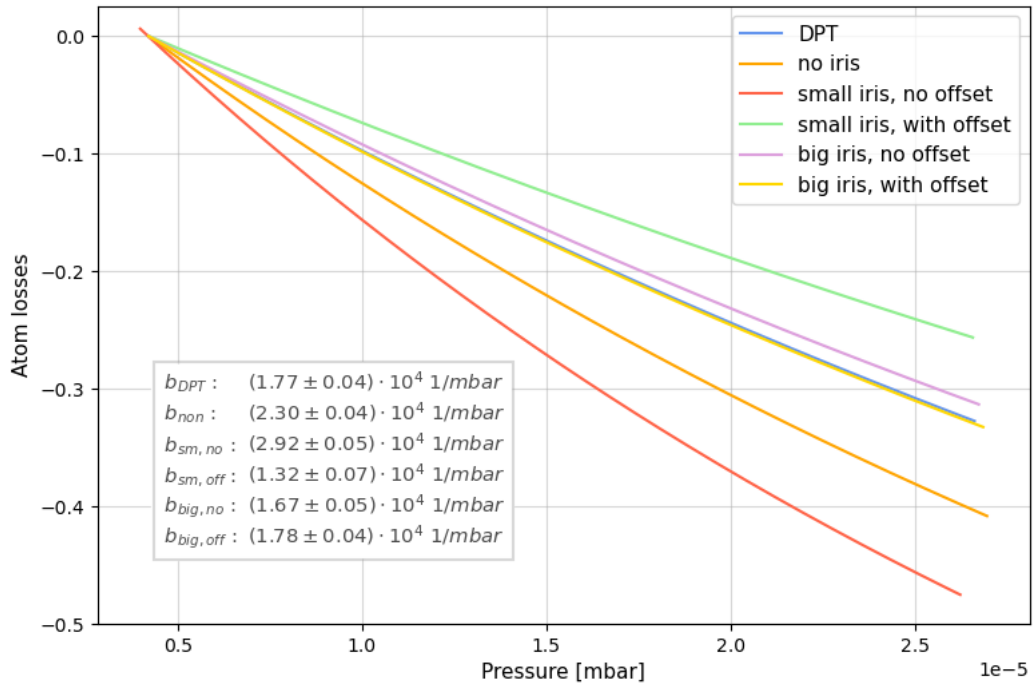

Figure 16: Pressure-dependent losses in the atom flux for all iris configurations. Based on the fitting model in eq. 4.2, the deviation of the data from their natural curve without scattering is depicted. It was assumed that for the lowest pressure there was no scattering and hence no atom losses.

of uncertainty arises from the evaluation method for fitting the model outlined in eq. 4.2. The fit parameters a and b are not completely decoupled in terms of describing the overall atom flux and the scattering rate. Elevating a also broadens the curve and shifts the drop to higher pressures which has to be compensated by a high b. For this reason, the seemingly low errors of b must be taken with caution across all configurations. In case of the small iris without offset configuration, thus, the smaller overall flux also seems to be unwillingly equalised with a higher end-to-end scattering, resulting in a misleading high b-parameter. Achieving a complete decoupling of these two degrees of freedom in the data evaluation was not possible within the scope of this thesis.

All in all, the work of this thesis did show that it is possible to resolve differences in the quench flux for different iris configurations by help of an absorption measurement setup. Nevertheless, due to the high uncertainty in data reproducibility, ranking the configurations against each other is not feasible based on this measurement. For example, the small iris setups with and without offset showed big differences in their quench flux which seem to be very questionable, particularly when compared to the relatively similar quench flux of the two big iris setups.

Further conclusions related to this measurement are denoted in section 5.

5 Summary and Conclusion

ArTTA detects the noble gas radioisotope ^{39}Ar by using Atom Trap Trace Analysis for dating water and ice samples. This knowledge helps to further examine groundwater systems and ocean circulation, as well as the history of glaciers.

The experiment uses laser cooling to trap metastable ^{39}Ar in a MOT where it can further be detected. Providing an elevated count rate is crucial for the precision of the measurements since the extremely low abundance of the isotope is already very challenging. An evident step for increasing the count rate is enlarging the diameter of the smallest restriction in the apparatus, resulting in an enhanced throughput of atoms. However, this effect competes with a concurrent gain in scattering with background gas since the overall pressure rises simultaneously. Since scattering might represent a crucial limitation for a future optimizations of the vacuum system , the occurrence of scattering and how it can be minimised needs to be further investigated, which is done by this thesis.

If a metastable atom scatters with background gas, it deexites back to its ground state and is hence considered lost, as only metastable atoms can be detected in the MOT. This implies that especially the effect of scattering gains with increasing pressure. Investigating a simulated pressure profile of the current apparatus along the beam axis revealed that within the DPT connecting the source chamber and the subsequent MOL chamber the pressure is problematically high. In conclusion, modifications on the vacuum system in that location have great potential for improving the overall performance of the apparatus.

Therefore, within the frame of this work, six different vacuum configurations were installed at the back wall of the source chamber and further investigated, with the aim of understanding different correlations between configuration parameter and scattering rate. The range of configurations comprise a DPT (as in the previous system), four different iris setups and one without any restriction, thus no iris or DPT. For each configuration, the metastable atom flux was monitored before and after, to hence resolve losses due to scattering. The latter was executed by an already existing setup for measurements of the metastable argon flux in the quench chamber, also named quench flux. To quantify the pre-flux, an absorption setup was designed and placed directly behind the plasma source. It allows to steadily check the initial flux to guarantee similar conditions for the performed measurements and hence comparability. This is crucial since the plasma source changes its spatial mode at times which affects the output of metastable atoms.

The measurement accomplished resolving the quench flux for different pressures. It was found that for lower pressures, the quench flux arises almost linearly with increasing pressure. With higher pressures, the slope flattens out and for almost every configuration, the quench flux even starts to decline at some point. An established model was introduced as fit function that showed to effectively reproduce the observed quench data. It was intended that two

distinct fit parameters would describe the total atom flux and the scattering rate separately. However, the two parameters turned out to be strongly coupled. Further improvements on the model are therefore given as an outlook with the aim of maintaining a fit parameter that reliably describes the scattering rate. Moreover, overall atom flux of the model is based on the absorption measurement data. Developing a solid model describing the absorption signal would further contribute to a higher accuracy of the fits and is therefore left for future works.

It should be noted that because performing the measurements is extremely complex, repeating these measurement cycles is a crucial step.
The measurement data shows a reduction in flux for higher pressures, supporting the validity of the initial hypothesis that the impact of scattering gains with higher pressures, limiting the atom flux. The measurement shows that in case of the DPT, no elevated scattering was measured, although it comprises a very low conductivity due to its length and small diameter. It was furthermore tried out to install an iris with an offset to the back wall of the source chamber due to the assumption that this would elevate the probability of scattered atoms finding their way out of the tube in comparison to an installation without offset. This would lower the pressure inside the connecting tube and hence lead to a reduction of scattering. However, no reliable distinction between the two configurations could be drawn from the measurement data which suggests that adding an offset has no significant effect on the scattering rate.

Evaluating the data of the configurations with larger diameters was of great interest, since an evident step to achieve an increase in the count rate would be the enlargement of the diameter of the smallest tube, which restricts the atom flux. As there was no anticipated elevated scattering resolved, the possibility is provided to expand the diameter in this section of the vacuum system, enabling a higher overall atom flux which could potentially yield a significant increase in the count rate. However, it further has to be considered that the optimization the vacuum system cannot solely rely on these scattering measurements. For a full evaluation of the different performances, investigating the whole apparatus is necessary. The iris configuration affects the pressure profile in the further apparatus, up to the MOT chamber. Since the mean lifetime of trapped atoms in the MOT has a 1/p-dependency, maintaining the pressure as low as possible is crucial for the count rate. Hence, tracking the pressure in the MOT chamber for different iris configuration would provide valuable data for conducting further investigations in terms of optimizing the vacuum system. These modifications to the apparatus hold significant importance due to their consistent and enduring impact.

A Appendix

A.1 Modification of the model for quantification of losses

The pressure profile along the position z on the beam axis depends on the set pressure in the source chamber p_0. In approximation, p_0 is defined as the offset of the pressure profile, resulting from testing different source chamber pressures within an unpublished simulation [24] of the vacuum system of ArTTA. The dependency of the pressure on the position z is comprised in $p^*(z)$.

$$p(z) = p(p_0, z) = p^*(z) + p_0 \tag{A.1}$$

Inserting this approximated pressure profile into the integral in the model in eq. 4.1 yields

$$\begin{aligned} \int_0^z \frac{1}{\lambda(z')}\, dz' &= \frac{\sigma}{k_B T_{bg}} \cdot \int_0^z p(z') dz' = \frac{\sigma}{k_B T_{bg}} \cdot \int_0^z \left(p^*(z) + p_0\right)\right) dz' \\ &= \frac{\sigma}{k_B T_{bg}} \cdot \left(\int_0^z p^*(z) dz' + \int_0^z p_0 dz' \right) = b_1(z) + b_2(z) \cdot p_0 \end{aligned} \tag{A.2}$$

Since the position z is fixed in the measurements, the pressure in the source chamber p_0 (further denoted as $p_0 = p$) is the only parameter varied within a measurement cycle. Therefore, the atom flux is given by $I(z) \to I(p)$ and $b_1(z) = b_1$ as well as $b_2(z) = b_2$.

As already said, the fit function for the absorption signal follows the model

$$I_0^{abs}(p) = A\, p\, \exp\left(-B\, p^2\right) + C \tag{A.3}$$

where A, B and C are fit parameters.

The overall atom flux I_0 in 4.1, also depending of the pressure, is assumed to be proportional to the measured absorption signal, hence $I_0 = I_0(p) = a_1 \cdot I_0^{abs}(p)$, with $a_1 \in \mathbb{R}$.

Inserting the initial atom flux and the simplification from eq. A.2 in the model of 4.1 yields:

$$\begin{aligned} I(p) &= a_1\, I_0^{abs}(p)\, \exp\left(-\left(b_1 + b_2 p\right)\right) = \left[a_1\, \exp\left(-b_1\right)\right] \cdot I_0^{abs}(p)\, \cdot\, \exp\left(-b_2 p\right) \\ &= a\, I_0^{abs}(p)\, \exp\left(-b\, p\right) \end{aligned} \tag{A.4}$$

In the last line, $a = a_1\, \exp\left(-b_1\right)$ and $b = b_2$ were redefined.

For the final fit, an offset parameter c is added. This is common for fitting to experimental data.

$$I(p) = a\, I_0^{abs}(p)\, \exp\left(-b\, p\right) + c \tag{A.5}$$

A.2 Collisional cross section

The cross section for collisions σ can be calculated, using the following formula:

$$\sigma = \pi(r_1 + r_2)^2 \tag{A.6}$$

whereby r_1 and r_2 are the radii of the two atoms participating in the collision.

Collisions of ground state argon atoms and metastable argon atoms are of interest for this theses. With the given radii $r_g = 188\text{pm}$ and $r_m = 789\text{pm}$ (taken from [15]), the cross section for different scattering processes can be determined:

$$\begin{aligned} \sigma_{gg} &= 44\,\text{Å} \\ \sigma_{gm} &= 300\,\text{Å} \\ \sigma_{mm} &= 782\,\text{Å} \end{aligned} \tag{A.7}$$

The cross section of collisions between of metastable atoms with neutral background gas, speaking of ground state argon atoms, is about a factor 6 bigger than the collisional cross section between two ground state argon atoms.

Bibliography

[1] O. A. Schaeffer R. W. Stoenner and S. Katcoff. Half-lives of argon-37, argon-39, and argon-42. *Science 148.3675 (1965), pp. 1325–1328*. doi: 10.1126/science.148.3675.1325.

[2] J. Chen. Nuclear data sheets for a=39. *Nuclear Data Sheets 149*, 149 (2018), pp. 1-251. ISSN 0090-3752. doi: 10.1016/j.nds.2018.03.001.

[3] Ph Collon et al. Development of an ams method to study oceanic circulation characteristics using cosmogenic ^{39}ar. *Nuclear Instruments and Methods in Physics Research Section B: Beam Interactions with Materials and Atoms*, 223-224 (2004). Proceedings of the Ninth International Conference on Accelerator Mass Spectrometry, pp. 428–434. ISSN 0168-583X. doi: 10.1016/j.nimb.2004.04.081.

[4] Verena Oehmke. *Zeeman Slower in Argon Trap Trace Analysis*. Heidelberg, 2023.

[5] Andrea M. Mitofsky. *DIRECT ENERGY*. URL https://eng.libretexts.org/Bookshelves/Electrical_Engineering/Electro-Optics/Direct_Energy_(Mitofsky)/07%3A_Lamps%2C_LEDs%2C_and_Lasers/7.01%3A_Absorption%2C_Spontaneous_Emission%2C_Stimulated_Emission.

[6] H.J. Metcalf, P. Van der Straten, J.L. Birman, J.W. Lynn, H.E. Stanley, M.P. Silverman, and M. Voloshin. *Laser Cooling and Trapping*. Graduate texts in contemporary physics. Springer, 1999. ISBN 9780387987477. URL https://books.google.de/books?id=i-40VaXqrj0C.

[7] Florian Ritterbusch. *Realization of a collimated beam of metastable atoms for ATTA of Argon 39*. Heidelberg, 2009.

[8] Julian Frederick Robertz. *Refining Argon Trap Trace Analysis - Crucial Features and Characterization Tools for Reliable Routine Measurements*. Heidelberg, 2023.

[9] Lasse Kundy. *Argon Trap Trace Analysis - Improved Transverse Laser Cooling and Investigation of Repumper Frequencies*. Heidelberg, 2023.

[10] Hidetoshi Katori and Fujio Shimizu. Lifetime measurement of the $1s_5$ metastable state of argon and krypton with a magneto-optical trap". *Phys. Rev. Lett. 70*, 23 June 1993. doi: 10.1103/PhysRevLett.70.3545.

[11] Sven Ebser. *Dating of ice and ocean samples with atom trap trace analysis of 39Ar*. Heidelberg, 2018. doi: 10.11588/heidok.00024512. URL http://nbn-resolving.de/urn:nbn:de:bsz:16-heidok-245121. Die Zahl 39 ist im Titel hochgestellt.

[12] Lisa Ringena. *Demonstration of a Dual Atom Trap Trace Analysis Setup for 39Ar and 85Kr*. Heidelberg, 2021. Die Zahlen 39 und 85 sind im Titel hochgestellt.

[13] 10/02/2024. URL https://www.pfeiffer-vacuum.com/en/know-how/introduction-to-vacuum-technology/fundamentals/.

[14] Tomio Okada Sugawara. Determination of ionization cross section for argon metastable-metastable collision by means of afterglow technique. *Japanese Journal of Applied Physics*, 35(8R):4535, aug 1996. doi: 10.1143/JJAP.35.4535. URL https://dx.doi.org/10.1143/JJAP.35.4535.

[15] J. Welte. *Atom Trap Trace Analysis of 39Ar*. Heidelberg, 2011. Die Zahl 39 ist im Titel hochgestellt.

[16] R. Gordon Livesey. Flow of gases through tubes and orifices.

[17] G. Vandoni. *THE BASIS of VACUUM*. 2012.

[18] Niclas Valentino Mandaric. *Characterization of the spatially dependent metastable argon production in a RF-discharge source*. Heidelberg, 2022.

[19] Lisa Eileen Moraw. *Optischer Aufbau der 2D magneto-optischen Falle*. Heidelberg, 2023.

[20] 28/02/2024. URL https://www.thorlabs.com/newgrouppage9.cfm?objectgroup_id=6207.

[21] Dr. Susanne Pahlow Dr. Thomas G. Mayerhöfer and Prof. Dr. Jürgen Popp. *The Bouguer-Beer-Lambert Law: Shining Light on the Obscure*. 2020. URL https://www.ncbi.nlm.nih.gov/pmc/articles/PMC7540309/.

[22] 01/02/2024. URL https://www.idealvac.com/files/manuals/Pfeiffer_CenterLine_ITR_90_FullRange_Pirani_Bayard_Alpert_Gauge_Operating_Instructions.pdf.

[23] Ohio State University, 18/02/2024. URL https://www.asc.ohio-state.edu/gan.1/teaching/spring04/Chapter4.pdf.

[24] Carl Kindermann. Master thesis. Unpublished.

Acknowledgements

Final möchte ich mich nochmal bei allen bedanken, die mich das letzte halbe Jahr begleitet haben und zu einer so schönen Zeit gemacht haben. Ich habe sehr viel gelernt und vor allem habe ich den Spaß an der Arbeit am Experiment gefunden. Es war sehr spannend, zum ersten Mal in einem Labor zu stehen und mitzubekommen, was über den Hörsälen der Uni so stattfindet. Außerdem war es im Fall von ArTTA 2 unglaublich cool, live dabei gewesen zu sein, wie ein ganzes Labor neu aufgebaut wurde. Im Herbst ist das Labor aus einem Container neben dem KIP in den 2. Stock des Gebäudes gezogen. Und während wir im September noch Deckenregale geschraubt und Kabel verlegt haben, wurden jetzt im Februar schon die ersten Zählraten gemessen. Ist das nicht cool!

Lieber Markus, vielen Dank, dass ich ein Teil der ArTTA-Gruppe werden durfte und danke, dass du immer mit viel Freude und Leidenschaft an den Projekten dabei bist.
Lieber Werner, vielen Dank, dass du Zweitprüfer dieser Arbeit bist.

Liebes ArTTA-Team, vielen Dank, dass es immer so viel Spaß gemacht hat, mit euch zu arbeiten und man immer gerne ins Büro gekommen ist. Ich weiß es auch sehr zu schätzen, dass ihr alle so hilfsbereit seid und jeder für gute Laune im Büro gesorgt hat.
Ein besonderer Dank geht an Carl, dafür dass ich jederzeit auf dich zukommen konnte und du mir immer sehr weitergeholfen hast.
Ein großes Dankeschön an David, dafür dass du immer die richtigen Tipps parat hattest und ich viel von dir lernen konnte.
Vielen Dank an Julian, dass du mich so lehrreich ins Labor eingeführt hast.

Ein besonderer Dank geht an Carl, David und Nikolas für das Korrekturlesen meiner Arbeit.
Vielen Dank Nikolas, dass du mit deiner Leidenschaft für die Physik inspirierst und immer gute Stimmung im Stockwerk verbreitest.

Vielen Dank auch an das gesamte 2. Stockwerk des KIP dafür, dass es dank euch so viel Spaß gemacht hat, jeden Tag an die Uni zu kommen. Ich habe alle Kaffeepausen in der Frühstücksecke sehr genossen.

Ein ganz großes Danke auch an Anni, Bela und Michi dafür, dass ich immer auf euch zählen kann und ihr die Zeit auch außerhalb der Uni so schön gestaltet habt.
Vielen Dank auch an meine Familie, dafür dass ihr immer für mich da seid und mich bei allem tatkräftig unterstützt.

Erklärung

Ich, Lisa Eileen Moraw, versichere, dass ich diese Arbeit selbstständig verfasst habe und keine anderen als die angegebenen Quellen und Hilfsmittel benutzt habe.

Heidelberg, den 29. Februar 2024